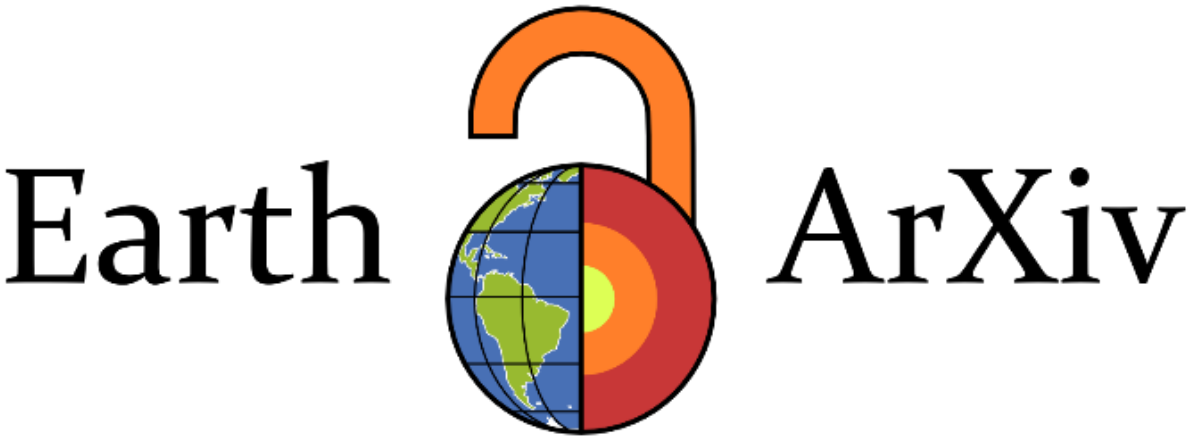

Peer review status:

This is a non-peer-reviewed preprint submitted to EarthArXiv.

Sijmen Zwarts S.Zwarts@tudelft.nl
Winston Lindqwister W.Lindqwister@tudelft.nl
Martin Lesueur M.Lesueur@tudelft.nl

Database of Generated Rock Microstructures and their computed Geometrical and Hydraulic properties

Sijmen Zwarts[a,*], Winston Lindqwister[a], Martin Lesueur[a]

[a] *Civil Engineering and Geosciences, Delft University of Technology, Delft, Netherlands*

Abstract

There is a strong link between a material's microstructural features and its macroscopic physical properties. However, heterogeneities in real-world rock microstructures often result in strong cross-correlations between the microscopic features, making it difficult to evaluate the influence of individual characteristics. Minkowski functionals (MFs), a set of measures derived from integral geometry, have recently gained attention as a robust way to quantify microstructural features. Recent datasets include the computed MFs to study their influence, but typically lack variation in individual MFs and offer limited ability to isolate specific contributions. Therefore, we present a curated, open-source dataset of microstructures, including random packings with varying grain shapes and cemented configurations featuring complex void networks. For each microstructure, the corresponding MFs are computed alongside the results of Stokes flow simulations. The controlled variation in particle shape and packing fraction enables a broader range of MFs, allowing for targeted analysis of how specific microstructural features influence macroscopic properties. This dataset supports the development and validation of structure–property models.

Keywords: Rock microstructures, Porous Media, Permeability, Fluid flow, Minkowski functionals

1. Background

A strong correlation exists between the microstructural features of a material and its macroscopic physical properties. This understanding has led to numerous studies aimed at investigating all types of microstructural properties that could be measured. For example, in geomaterials, properties such as grain shape, grain roughness, and porosity strongly influence mechanical (Klinkmüller et al., 2016; Zhao et al., 2021; Huang et al., 2023; Nouguier-Lehon et al., 2003; Hatefi et al., 2024; Carrasco et al., 2025) and hydraulic behavior (Tillmann et al., 2008; Dolinar, 2009; Vienken and Dietrich, 2011; Zieba, 2016; Zhao et al., 2020; Rezaei et al., 2021), while in energy materials, similar microstructural features affect electrical performance (GUO and WASER, 2006; Belal Hossen and Akther Hossain, 2015; Ghayour and Abdellahi, 2016; Bansal et al., 2020;

*Corresponding author
Email address: s.zwarts@tudeltf.nl (Sijmen Zwarts)

Gomaa, 2020; Kaliyaperumal et al., 2023; Gomaa, 2025). To better understand these structure–property relationships, researchers have increasingly turned to large databases of microstructures (Röding et al., 2020; Santos et al., 2022; Avilkin et al., 2025; Prodanovic et al., 2025) where microstructural properties vary depending on rock samples and rock types.

Real-world microstructures, however, inherently exhibit heterogeneities in the distribution of microscale features, such as grain morphology and spatial arrangement. These heterogeneities complicate efforts to isolate the influence of individual features on macroscopic behaviour. In many cases, the resulting structural complexity leads to cross-correlations between properties. For instance, increased surface roughness often coincides with variations in porosity, making it difficult to establish causal relationships between specific microstructural characteristics and observed physical properties.

To enable a more robust understanding of these structure–property relationships, the microstructure must be thoroughly quantified. Standard descriptors, such as porosity, particle size distribution orientation, and particle shape, are commonly used in characterizing porous media, but are often correlated and only specific to granular materials. The more generic use of porosity also falls short as, for example, they do not adequately capture the connectivity of the pore space, which is critical for fluid transport, nor the continuity of the solid matrix, which underpins mechanical strength. A more rigorous methodology to quantify these topological and geometrical features, which is introduced in recent research, are Minkowski Functionals (MFs) (Santaló and Kac, 2004; Schneider, 2014; Armstrong et al., 2018). MFs are a set of functionals, coming from integral geometry, which allows for a necessary and sufficient characterization of the geometry and topology of an image, assuming the image is motion invariant or isotropic. The functionals are the porosity, material matrix surface area, mean curvature and the Euler characteristic, from which the latter is directly related to the connectivity of the pore network (Scholz et al., 2012; Herring et al., 2019). The MFs enable a generalised and systematic quantification of microstructural features. An additional advantage of MFs is that the values are easily obtained, measured directly on the segmented μCT images of rock microstructures.

Some studies have tried to couple the MFs to the physical properties and by doing that created their own databases of microstructures with the MFs included (Lindqwister et al., 2025b). However, these generated microstructures still influence the different MFs simultaneously. Therefore, researchers need to first consider idealised microstructures in order to test the influence of individual microstructural characteristics (Lindqwister et al., 2025a). These simplified microstructures enable a controlled variation of the microstructural of specific features, such as grain shape and size distribution. Random packings offer a systematic approach to create granular idealized microstructures based on the packing fraction of particles, which controls the porosity of the structure, while perfectly circular particles eliminate grain roughness of the grains. Many experimental studies use glass beads to isolate the porosity and grain diameter to study the hydraulic or mechanical properties (Lu et al., 1994; Říha et al., 2018; Herring et al., 2019; Carbillet et al., 2021). Numerical studies complement these experiments by enabling the study of microstructure–property relationships in a fully non-destructive and controlled environment. They allow researchers to introduce and analyse microstructural complexity beyond what is easily achievable in physical experiments. Those random packings are for example widely employed in Representative Elementary Volume (REV) conver-

gence studies (Du and Ostoja-Starzewski, 2006; Zwarts and Lesueur, 2024b), which are essential for assessing the size and structure required for rigorous upscaling of material properties in simulations.

As can be noted from all references, researchers often rely on their own numerically generated data. As a consequence, the dataset is often limited in terms of variations of the different geometrical and topological properties. This prevents structure-property models being developed from being thoroughly validated by testing against a large range of microstructures. The influence of certain properties is also difficult to perceive without a dataset that allows one to isolate those specific properties. Indeed, despite the interest in linking microstructural characteristics to macroscopic properties, there remains a lack of a large, coherent dataset with a large variation of the individual MFs and the ability to isolate each of them. This limits the ability to rigorously evaluate and develop models to study the influence of both the physical and numerical quantities.

This work presents a curated database of idealized microstructures designed to enable systematic investigation of microstructure–property relationships. The dataset includes granular microstructures, spanning a wide range of grain shapes and packing fractions to generate broad variability in the associated MFs. This variability facilitates the isolation of individual MF effects on macroscopic properties. Beyond random packings, the database also incorporates cemented microstructures with more complex void networks that better approximate the channel morphology found in real rocks. For each microstructure, we provide computed Minkowski Functionals, as well as data on homogenized hydraulic conductivity and microscale flow energetics, which allows for direct correlation studies between microstructural descriptors and permeability. The dataset supports consistent use of idealized microstructures across numerical studies. Additionally, the large number of samples makes the database particularly suitable for training machine learning models aimed at predicting effective properties from microstructural geometry. The availability of user-friendly source code allows future users to add new entries to the database to grow it even larger and widen its scope.

2. Material and methods

2.1. Minkowski functionals

Minkowski functionals (MFs) are a set of measures used to quantify the geometric and topological features of a structure, including shape, convexity, and connectivity. These characteristics are particularly relevant at the microstructural level, making MFs a promising tool for linking microstructure to physical properties (Santaló and Kac, 2004; Schneider, 2014; Armstrong et al., 2018). Derived from integral geometry, MFs provide a general and mathematically rigorous framework for describing complex structures. Their additive nature makes them especially well-suited for digital image analysis, enabling consistent characterisation across scales and configurations.

Here, the basic formulations and theorems of the Minkowski functionals are presented, while more detailed treatments can be found in the referenced works. Consider a microstructure with a solid body Ω, bounded by a surface $\partial\Omega$, in an n-dimensional Euclidean space. The integral geometry provides that $n+1$ functionals are needed to describe the geometry and topology of the microstructure in its completion. The first functional is

the total volume of the body, described by:

$$M_0 = \int_{\Omega} dV \tag{1}$$

Note that in the case of this dataset, the point of view starts from the pore-space. Hence, the normalised value of the first Minkowski functional is equivalent to the porosity commonly used in the Digital Rock Physics framework (Saxena et al., 2019). The second functional is the integral measure of the surface area of the body, defined as:

$$M_1 = \int_{\partial\Omega} dS \tag{2}$$

In which dS is the boundary of the surface elements in the microstructure. The third integral, applicable in a three-dimensional case, represents the mean curvature of the sample, described as:

$$M_2 = \int_{\partial\Omega} \left(\frac{1}{r_1} + \frac{1}{r_2} \right) dS \tag{3}$$

Here r_1 and r_2 are the principal radii of curvature of the surface elements of the body in the different axis. The last Minkowski functional is the Gaussian curvature of the surface, which is linked to the topology of the microstructure via the Gauss-Bonnet theorem (do Carmo, 1976).

$$M_3 = \int_{\partial\Omega} \left(\frac{1}{r_1 r_2} \right) dS = 4\pi\chi(\Omega) \tag{4}$$

Where $\chi(\Omega)$ is the Euler characteristic of the solid object. The Euler characteristic can also be found by the sum of the number of objects and cavities, minus the number of redundant loops. In the datasets of granular packings, it is assumed that the grains are impermeable and therefore are created without any intrinsic porosity, which means that the Euler characteristics are equal to the number of particles. A graphical overview of all the Minkowski functionals is provided in Fig. 1.

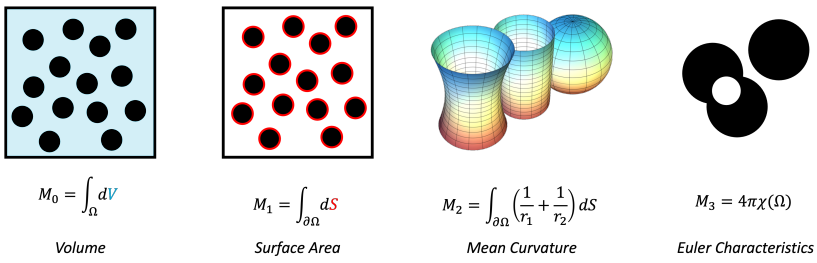

Figure 1: A graphical representation of the different Minkowski Functions, from the pore spaces' point of view.

The second Minkowski functional, corresponding to the mean curvature in 3D, does not have a direct 2D equivalent. In 2D, only three Minkowski functionals are defined: area, perimeter, and Euler characteristic.

2.2. Digital computation of Minkowski Functionals

To compute MFs from digital representations of the microstructures, we adopt a voxel-based approach. Each microstructure is represented as a two-dimensional binary image, where the pore space and the solid matrix are denoted by 1 and 0, respectively. The following procedure is used to extract the Minkowski functionals:

- M_0: Porosity
  The zeroth Minkowski functional corresponds to the volume (or area, in 2D) of the pore phase and is computed as the ratio of pore voxels to the total number of voxels. This is implemented using `ps.metrics.porosity(binarised)`, where `binarised` is the binary image of the microstructure. It returns the scalar porosity:

$$M_0 = \frac{N_{\text{pore}}}{N_{\text{total}}}$$

  which provides a basic measure of void space in the material.

- M_1: Surface area
  The first Minkowski functional is the surface area (or in 2D the perimeter) between solid and pore space. We estimate this using the Crofton formula (Cayley, 1868) via the `perimeter_crofton(im_inv, directions=8)` function, implemented in scikit (van der Walt et al., 2014), where `im_inv` is the inverse binary image. The perimeter is estimated by counting intersections with lines from multiple directions:

$$M_1 = \texttt{perimeter\_crofton(im\_inv, directions=4)}$$

  For consistent measurement of the length, the image is normalised to have a unitary length in each direction. There is the option to choose between algorithms that determine continuity in the matrix in 4 or 8 directions, either including the diagonal pixels or not. We found the best consistency with the exact analytical solution for random packings with `directions=4`. and apply those to other microstructures as well.

- M_2: Mean Curvature:
  The second Minkowski functional corresponds to the mean curvature, which is only defined in 3D. We estimate it by first extracting the surface mesh of the pore space using a marching cubes algorithm on the binary voxel data. The mean curvature at each vertex of the mesh is then computed using the curvature function of pyvista (Sullivan and Kaszynski, 2019). The mean curvature is integrated over the entire surface by averaging over each triangular face and weighting by its area.

- M_3: Euler Characteristic
  The third Minkowski functional corresponds to the Euler characteristic, which measures the connectivity of the pore network. It is computed using `euler_number(im_inv)` from scikit (van der Walt et al., 2014), where the inverse image `im_inv` ensures that solid structures are counted as objects. The Euler number is defined as:

$$M_3 = \chi = \#\text{objects} - \#\text{holes}$$

The function checks the connectivity of the voxels and, from that determines the number of objects and wholes, which leads to the Euler Characteristic. When working with granular materials, it is assumed that the grains are impermeable, and therefore the Euler Characteristic of those microstructures is equal to the number of particles. Similar to the perimeter, we use `directions=4`.

2.3. Generating Microstructures

2.3.1. Two-dimensional Random Packings

The microstructures consist of two-dimensional random packings of non-overlapping circles of equal size, created with PoreSpy (Gostick et al., 2019). During generation, the packing fraction is set to control the porosity, and the random seed is varied to obtain a statistically representative ensemble of samples. As a counterpart to the random packings, a structured microstructure is also generated for each packing fraction, where particles are arranged on a regular grid. This supplementary dataset allows to directly test the effect of microstructure randomness.

In the circular particle packings, the Minkowski functionals (MFs) are inherently coupled due to the fixed grain shape. Specifically, the number of particles M_3 is controlled by the packing fraction, which in turn directly determines the porosity $M_0 = \pi r^2 M_3$ and the surface area $M_1 = 2\pi r M_3$. This tight correlation limits the ability to study the independent effect of each MF.

To overcome this limitation, additional packings are generated using the same circle configurations as a base, but with particles of different shapes inscribed within each circle, namely rectangles, triangles, and ellipses, as shown in Fig. 2. These alternate shapes are defined by adjustable parameters such as aspect ratio (for rectangles and ellipses) and skewness (for triangles), while ensuring the particles remain non-overlapping. For example, a lower aspect ratio in ellipses or rectangles reduces M_0 and decreases M_1, while in triangles, the skewness parameter φ alters both the packed area and the surface area per particle. In addition, the overall packing fraction provides a global control on M_0 that is independent of the particle shape.

Taken together, these variations in grain geometry expand the accessible range of Minkowski functionals within the dataset. More importantly, they partially decouple the functionals: for instance, M_3 can be held constant (as defined by the original circle packing) while M_0 and M_1 vary with shape. Likewise, a given M_1 may correspond to different particle counts and porosities. This MF control allows us to investigate the influence of individual MFs in isolation.

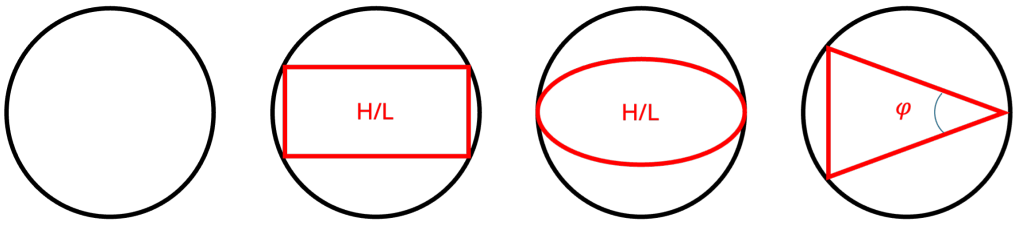

Figure 2: Abstract visualisation of how the different grain shapes are fitted. The rectangular and elliptical shapes depend on the ratio of the height and length. The triangular grains depend on the angle of the triangle shown as φ.

While the circle packings are an idealised representation of granular material which does not change by rotating the individual particle shape, the other grain shapes introduce a directional aspect to the shape packings. To allow for the study of this anisotropy, both a random distribution of grain orientation and an aligned orientation of all grains based on a certain angle (β) are included. In both configurations, the rotation of each particle is performed from the centre of the circle to ensure that the different particles still inscribe the original circle, preserving the original non-overlapping property of the circle. An example of the resulting inscription and rotation with the different grain shapes is shown in Fig. 3.

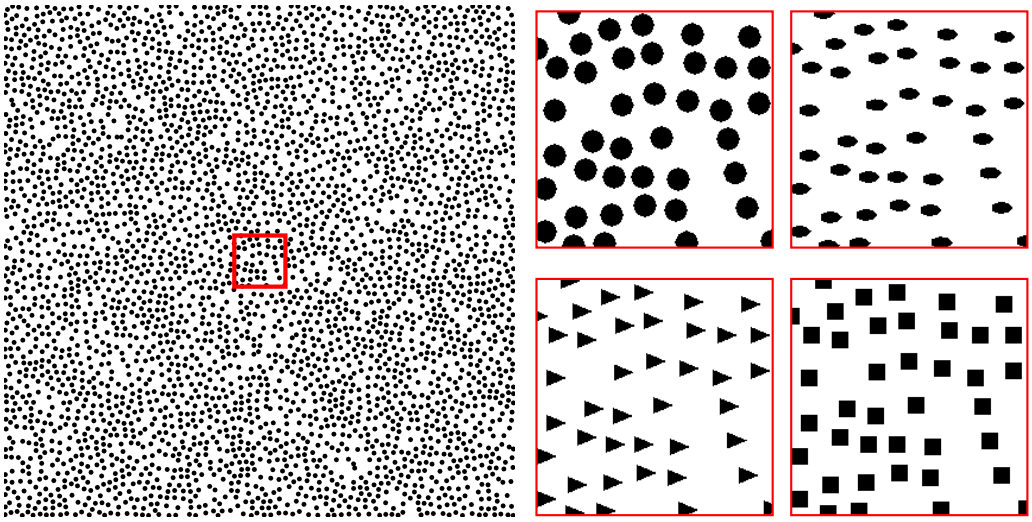

Figure 3: Example of the microstructure generation process. The left panel shows a representative random circle packing used as a baseline configuration. This packing is systematically converted into four different grain shapes —circles, ellipses, triangles, and rectangles, all oriented with the direction of the flow path— while preserving the spatial distribution. The right panel presents a zoomed-in 2×2 grid illustrating one example of each grain shape derived from the same initial packing.

In the previously described two-dimensional packings, the particle diameter of the original circle is fixed across all structures. To introduce further variability and to better approximate a two-dimensional cross-section of a three-dimensional porous material, we generate sphere packings using OpenMC (Romano et al., 2015) and Porespy (Gostick et al., 2019) and extract random cross-sections. These cross-sections naturally result in a distribution of particle sizes, as particles intersect the plane at different depths. This approach extends to non-spherical grains as well. Ellipsoidal particles are inscribed into the spherical cross-sections in the same way that ellipses are inscribed into circles in the 2D case. For cubical grains, however, a true two-dimensional cross-section would yield identical-sized rectangles, resembling the outcome of directly inscribing rectangles in circles. To increase the variance of the Minkowski functionals in this database, we generate supplementary samples where we relax the assumption of uniform grain size in three dimensions and inscribe rectangles of varying aspect ratios into the cross-section based on the effective radii observed in the two-dimensional slice.

2.3.2. Three-dimensional random packings

In addition to generating 2D cross-sections, the 3D sphere packings also allow for the direct construction of three-dimensional microstructures. To expand the dataset into 3D, we inscribe various grain shapes—including cubes, ellipsoids, and pyramids—within the spheres of the packing. This enables the study of shape-induced heterogeneity in fully three-dimensional domains and provides a more realistic representation of natural and engineered porous materials. These 3D structures complement the 2D dataset and support future work on volumetric Minkowski functionals, permeability tensors, and anisotropic transport phenomena.

2.3.3. Cemented microstructures

While the previously described microstructures consist of discrete, non-overlapping grains typical of granular media, real-world porous materials often consist of cemented structures in which individual grains are fused together. To capture such morphologies, an additional set of microstructures is generated using a "blob" model. These structures exhibit more continuous, channel-like pore geometries, which particularly resemble carbonate rocks. The blobs are created by applying a Gaussian blur to a field of random noise, followed by renormalisation to a uniform distribution using functionality available in PoreSpy (Gostick et al., 2019). This process results in a binary image representing the solid and void phases. Next to the porosity, the blobiness is varied in this dataset, which controls the size of the rock-like structure, as shown in Fig. 4.

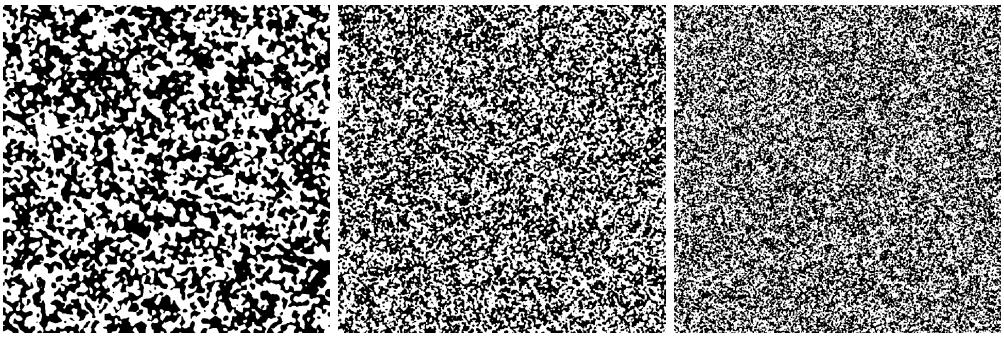

Figure 4: Three examples of generated cemented microstructures, controlled by the porosity and the size of the initial particles (blobiness). Black represents the material matrix in the microstructure and white the porosity. In this example, from left to right, a blobiness of 5, 10 and 15 are shown, all with a porosity of 50%.

2.4. Stokes-flow simulations

Once a random packing is generated, it is discretised and meshed using GMSH (Geuzaine and Remacle, 2008) into conforming triangular elements. The cemented structures are meshed with the in-built meshing of MOOSE (Giudicelli et al., 2024), based on a colour threshold. These meshes serve as the input for finite element simulations of steady-state incompressible fluid flow. Assuming negligible inertial and body forces, and constant viscosity, the governing equations result in the Stokes flow equations:

$$\mu \nabla^2 \mathbf{v} - \nabla P = 0 \tag{5}$$

$$\nabla \cdot v = 0 \tag{6}$$

where μ is the dynamic viscosity, $\mathbf{v}$ is the fluid velocity, and P is the pressure. These conditions are representative of low Reynolds number flow in porous or granular media such as subsurface environments. The simulations are implemented in the MOOSE framework (Peterson et al., 2018), following the setup of Lesueur et al. (2017). A unit viscosity is imposed, and a unit pressure drop is applied between the left and right boundaries of the domain to drive flow, while the top and bottom boundaries are set as no-flow. A no-slip condition is enforced on all solid-fluid interfaces to reflect the impermeability of the grains.

Postprocessing is based on the methodology described by Zwarts and Lesueur (2024a), in which spatial homogenization is applied in the center of the domain to extract effective quantities, minimizing the influence of boundary layers. From the spatially averaged velocity $\bar{\mathbf{v}}$, the intrinsic permeability K is obtained using Darcy's law:

$$K = \frac{\bar{v}\varphi}{\nabla P} \tag{7}$$

where φ is the porosity and ∇P is the imposed pressure gradient. The microscale energy dissipation E, a second quantity of interest, is computed as the scalar product of the velocity field with the pressure gradient:

$$E = \int_V \nabla P \cdot v \tag{8}$$

3. Data Records

As summarised in Table 1, a comprehensive set of two-dimensional microstructures was generated by systematically varying grain shape, orientation, size distribution, and size parameters. For each unique parameter combination, 25 random configurations were created to enable statistical analysis of microstructural variability. Additionally, one structured (regular) packing was generated per configuration to serve as a reference. The packing fraction with a homogeneous circle diameter was varied from 1% to 55% in 1% increments, providing fine-grained coverage of the full range of dilute to moderately dense microstructures. While the theoretical maximum packing fraction for circular particles approaches 91% in a hexagonal arrangement, we limit the upper bound to 55% to maintain computational feasibility and allow for efficient generation of diverse samples. Beyond this threshold, particle overlap constraints complexity significantly increase generation time without yielding proportional benefit for the intended statistical analysis. For the varying diameter, packing fractions varying from 7% to 62%, with increments of 5% are generated. As the samples come from a sphere-packing, in which the closed random packing limit is 64%. In total, the dataset comprises 82075 individual two-dimensional random packing samples.

Fig. 5 shows that the MF space originates from a reference point characterised by $M_0 = 1, M_1 = 0$ and $M3 = 0$ and evolves linearly along distinct trajectories depending on the microstructural configuration. Circular grain packings follow a single linear trend, determined by the radius of the particles. Introducing varied grain shapes leads to a broader distribution in MF space. By systematically varying shape parameters, we

Grain shape	Grain orientation	Grain size distribution	Size parameter
Circles	Random	Homogeneous Heterogeneous	-
Triangles	Random Aligned Perpendicular Diagonal	Homogeneous Heterogeneous	$\varphi =$ 25 30 35 40 45
Rectangles	Random Aligned Perpendicular Diagonal	Homogeneous Heterogeneous	$\frac{h}{L} =$ 0.5 0.66 0.75 1
Ellipses	Random Aligned Perpendicular Diagonal	Homogeneous Heterogeneous	$\frac{h}{L} =$ 0.5 0.66 0.75 1

Table 1: Summary of the contents of the 2D Random Packings in the dataset

observe changes in the directional slopes of the MF vector, suggesting the potential to span an octant of a sphere in the Minkowski space.

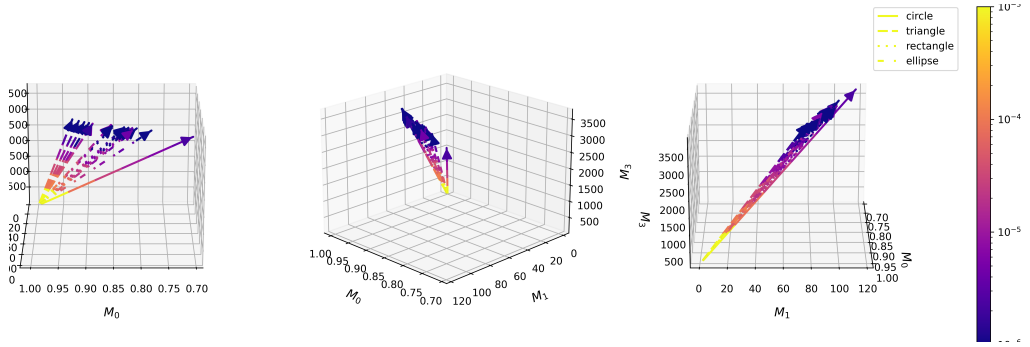

Figure 5: The MF space of the different random packings generated with different porosity and grain properties. The colours in the graph indicate the computed permeability of the samples on a log-normal scale.

For the blobs, samples span a wide porosity range, from 55% to 95%, in increments of 4.5%. Below a porosity of 50%, we obtain a negative Euler number (see Fig. 6) indicating a lack of percolation Sadeghnejad et al. (2023). For each porosity level, structures were generated with blobiness parameters varying from 10 to 15 in unit steps, selected to capture different degrees of pore-space smoothness, connectivity and a realistic range of microstructures. Each unique combination of porosity and blobiness results in 50 independently generated configurations. For each configuration, the sample is cut into 400 smaller subsamples for the postprocessing of the physical properties. Whereas the granular material had a MF space starting from the origin, the MF space for the cemented

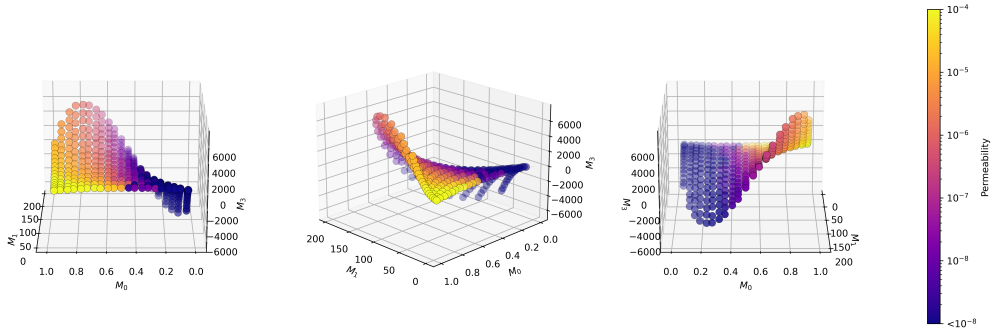

Figure 6: The MF space of different cemented microstructures generated with different porosity and blobiness, shown in 3 different view orientations. The colour scale indicates the dimensionless permeability of the samples, shown in a log-normal scale.

microstructures offer a different shaped plane, in which lower porosities correlate to a negative curvature compared to the surface area, and higher porosities correlate to a positive curvature. This contributes to a wider variation of the whole MF space and permeability.

4. Technical validation

To ensure the robustness and reliability of the dataset, several validation steps were performed.

4.1. Mesh independence

We verified the numerical stability of computed permeability values with respect to mesh resolution by performing mesh convergence tests for representative geometries. As shown in the example of Fig. 7, the permeability stabilises with increasing degrees of freedom (DOFs), indicating that the mesh density used in the final dataset is sufficient for accurate fluid flow simulations. This mesh-convergence study is performed for the different hydraulic properties and MFs.

4.2. REV convergence

Once the results of all the samples with the same characteristics have been gathered, a REV convergence study is applied to find the representative physical property of the microstructures, following the method from Zwarts and Lesueur (2024b). In summary, the physical properties are fitted into a log-normal distribution, from which we extract the variance for a sample with a reference size. This variance directly correlates to the variance of samples with different sizes, using the ratio of the sizes. This allows to fit a cone-shaped convergence law on the samples and extract the converged properties and size of the REV, which is provided in the following formula:

$$y = \mu \cdot \exp\left(\pm\sqrt{\frac{V_{ref}}{V_s}}\sigma_{ref}\right) \tag{9}$$

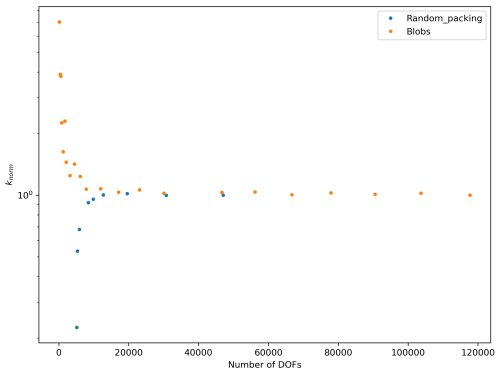

Figure 7: Mesh convergence study for the random packing (blue) and the blob microstructure (orange), shown in the permeability normalised to the last computed value. Once a certain number of degrees of freedom (DOFs) has been reached, the numerical solution converges to a value.

An example of the values of the standard deviation for each packing fraction for different properties is shown in Fig. 8. For each microstructure with the same characteristics, a REV convergence study of the MFs, permeability, hydraulic energy and tortuosity is provided.

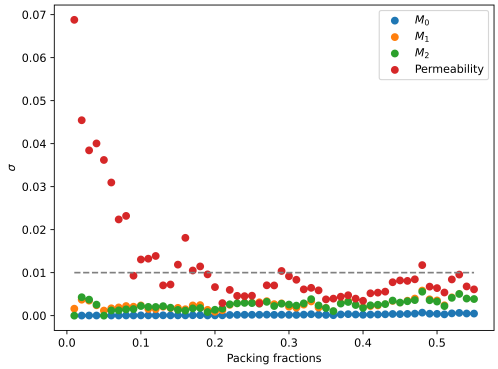

Figure 8: The standard deviation of the different packing fractions, compared to the different properties measured. In this image, an example of the random packing with triangular shapes is presented.

4.3. Permeability computation

For the validation of the hydraulic properties, we use the semi-analytical formulation of permeability of Kozeny-Carmen (Carman, 1939), which expresses the permeability in terms of the surface area S, porosity ε and shape factor k_z. Since the equation is based on Poiseuille's equation of flow through a tube and Darcy's law, we can express this both in two and three dimensions as:

$$k = \frac{\varepsilon^3}{k_z S^2} \tag{10}$$

Note that we don't use the specific surface area, usually estimated with $S = S_0(1-\varepsilon)$, as we measure the full surface area with the computation of the MFs. In two dimensions, we fit the shape factor, coming from the relation of the hydraulic radius to the representative channel height, to the circles and use that value with the other grain shapes values to compare the results of the simulations with the semi-analytical solution, as shown in Fig. 9. We find that the shape factor is around 14.

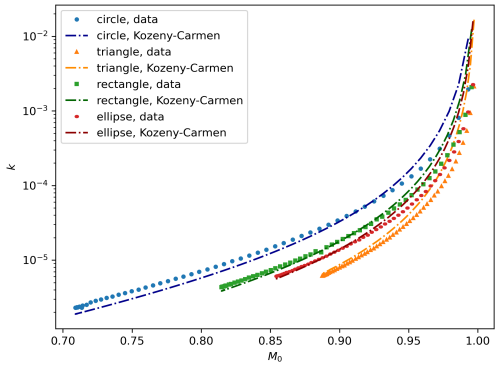

Figure 9: The permeability of the 2D random packing simulated samples, shown with markers, and the permeability as defined by the Kozeny-Carmen equation, shown with the dashed lines. The different grain shapes are presented in different colours.

5. Data availability

The database can be found in Zwarts et al. (2025), which is a github repository. Both the details of microstructures and results are shown there, supported by the scripts to generate the different microstructures.

6. Usage Notes

The microstructure-permeability database presented in this study spans a wide range of simulated 2D geometries and extracted transport properties, and can be found at Zwarts et al. (2025). The current dataset includes permeability computation, Minkowski functionals, and meshing details for each sample. Future updates —whether to incorporate new particle shapes, extend the parameter space (e.g., porosity or packing ratio), or include other physical properties— can be implemented with minimal effort by users.

7. Code availability

All scripts used for geometry generation, meshing, simulation, and data post-processing have been made publicly available in the associated repository Zwarts et al. (2025). These are modular and designed for reproducibility and traceability, allowing users to regenerate or extend the dataset seamlessly. We encourage community contributions to expand the dataset and improve upon the simulation and analysis routines.

Bibliography

Armstrong, R.T., McClure, J.E., Robins, V., Liu, Z., Arns, C.H., Schlüter, S., Berg, S., 2018. Porous media characterization using minkowski functionals: Theories, applications and future directions. Transport in Porous Media 130, 305–335. doi:10.1007/s11242-018-1201-4.

Avilkin, V., Olhin, A., Vishnyakov, A., 2025. Data-driven prediction of transport properties of porous media from pore cross sections on 2d images. Transport in Porous Media 152. doi:10.1007/s11242-025-02181-5.

Bansal, U., Singh, V., Brajesh, K., Gupta, R., Garg, A., 2020. Grain size dependence of electrical transport in magnetoelectric gallium ferrite ceramics. Journal of Alloys and Compounds 847, 156499. doi:10.1016/j.jallcom.2020.156499.

Belal Hossen, M., Akther Hossain, A.K.M., 2015. Complex impedance and electric modulus studies of magnetic ceramic ni0.27cu0.10zn0.63fe2o4. Journal of Advanced Ceramics 4, 217–225. doi:10.1007/s40145-015-0152-2.

Carbillet, L., Heap, M.J., Baud, P., Wadsworth, F.B., Reuschlé, T., 2021. Mechanical compaction of crustal analogs made of sintered glass beads: The influence of porosity and grain size. Journal of Geophysical Research: Solid Earth 126. doi:10.1029/2020jb021321.

Carman, P.C., 1939. Permeability of saturated sands, soils and clays. The Journal of Agricultural Science 29, 262–273. URL: https://www.cambridge.org/core/product/identifier/S0021859600051789/type/journal_article, doi:10.1017/S0021859600051789.

do Carmo, M.P., 1976. Differential Geometry of Curves and Surfaces. Prentice-Hall, Englewood Cliffs, NJ.

Carrasco, S., Cantor, D., Ovalle, C., Dubois, F., 2025. Particle shape distribution effects on the critical strength of granular materials. Computers and Geotechnics 177, 106896. doi:10.1016/j.compgeo.2024.106896.

Cayley, A., 1868. Second memoir on the curves which satisfy given conditions; the principle of correspondence. Philosophical Transactions of the Royal Society of London 158, 145–172. doi:10.1098/rstl.1868.0006.

Dolinar, B., 2009. Predicting the hydraulic conductivity of saturated clays using plasticity-value correlations. Applied Clay Science 45, 90–94. doi:10.1016/j.clay.2009.04.001.

Du, X., Ostoja-Starzewski, M., 2006. On the size of representative volume element for darcy law in random media. Proceedings of the Royal Society A: Mathematical, Physical and Engineering Sciences 462, 2949–2963. doi:10.1098/rspa.2006.1704.

Geuzaine, C., Remacle, J.F., 2008. An introduction to geometrical modelling and mesh generation with gmsh .

Ghayour, H., Abdellahi, M., 2016. A brief review of the effect of grain size variation on the electrical properties of batio3-based ceramics. Powder Technology 292, 84–93. doi:10.1016/j.powtec.2016.01.030.

Giudicelli, G., Lindsay, A., Harbour, L., Icenhour, C., Li, M., Hansel, J.E., German, P., Behne, P., Marin, O., Stogner, R.H., Miller, J.M., Schwen, D., Wang, Y., Munday, L., Schunert, S., Spencer, B.W., Yushu, D., Recuero, A., Prince, Z.M., Nezdyur, M., Hu, T., Miao, Y., Jung, Y.S., Matthews, C., Novak, A., Langley, B., Truster, T., Nobre, N., Alger, B., Andrš, D., Kong, F., Carlsen, R., Slaughter, A.E., Peterson, J.W., Gaston, D., Permann, C., 2024. 3.0 - MOOSE: Enabling massively parallel multiphysics simulations. SoftwareX 26, 101690. URL: https://www.sciencedirect.com/science/article/pii/S235271102400061X, doi:https://doi.org/10.1016/j.softx.2024.101690.

Gomaa, M.M., 2020. Heterogeneity in relation to electrical and mineralogical properties of hematitic sandstone samples. Applied Water Science 10. doi:10.1007/s13201-020-01186-3.

Gomaa, M.M., 2025. Effect of grain shape elongation in direction and perpendicular to current stream (conductive or insulator) on the electrical characteristics of mixtures. Scientific Reports 15. doi:10.1038/s41598-024-83223-8.

Gostick, J., Khan, Z., Tranter, T., Kok, M., Agnaou, M., Sadeghi, M., Jervis, R., 2019. Porespy: A python toolkit for quantitative analysis of porous media images. Journal of Open Source Software 4, 1296. doi:10.21105/joss.01296.

GUO, X., WASER, R., 2006. Electrical properties of the grain boundaries of oxygen ion conductors: Acceptor-doped zirconia and ceria. Progress in Materials Science 51, 151–210. doi:10.1016/j.pmatsci.2005.07.001.

Hatefi, M.H., Arabani, M., Payan, M., Zanganeh Ranjbar, P., Keawsawasvong, S., Jamsawang, P., 2024. The role of particle shape in the mechanical behavior of granular soils: A state-of-the-art review. Results in Engineering 24, 103572. doi:10.1016/j.rineng.2024.103572.

Herring, A.L., Robins, V., Sheppard, A.P., 2019. Topological persistence for relating microstructure and capillary fluid trapping in sandstones. Water Resources Research 55, 555–573. doi:10.1029/2018wr022780.

Huang, Q., Zhou, X., Liu, B., 2023. Effect of realistic shape on grain crushing for rounded and angular granular materials. Computers and Geotechnics 162, 105659. doi:10.1016/j.compgeo.2023.105659.

Kaliyaperumal, C., Marndi, S.K., Sankarakumar, A., Paramasivam, T., 2023. Physical insights into the grain size effect on the electrical properties of nanocrystalline la2zr2o7 pyrochlores. Ceramics International 49, 10663–10672. doi:10.1016/j.ceramint.2022.11.254.

Klinkmüller, M., Schreurs, G., Rosenau, M., Kemnitz, H., 2016. Properties of granular analogue model materials: A community wide survey. Tectonophysics 684, 23–38. doi:10.1016/j.tecto.2016.01.017.

Lesueur, M., Casadiego, M.C., Veveakis, M., Poulet, T., 2017. Modelling fluid-microstructure interaction on elasto-visco-plastic digital rocks. Geomechanics for Energy and the Environment 12, 1–13. doi:10.1016/j.gete.2017.08.001.

Lindqwister, W., Peloquin, J., Dalton, L.E., Gall, K., Veveakis, M., 2025a. Predicting compressive stress-strain behavior of elasto-plastic porous media via morphology-informed neural networks. Communications Engineering 4. doi:10.1038/s44172-025-00410-9.

Lindqwister, W., Veveakis, M., Lesueur, M., 2025b. Chemical homogenization for nonmixing reactive interfaces in porous media. ACS Omega 10, 21553–21567. doi:10.1021/acsomega.5c00641.

Lu, T.X., Biggar, J.W., Nielsen, D.R., 1994. Water movement in glass bead porous media: 2. experiments of infiltration and finger flow. Water Resources Research 30, 3283–3290. doi:10.1029/94wr00998.

Nouguier-Lehon, C., Cambou, B., Vincens, E., 2003. Influence of particle shape and angularity on the behaviour of granular materials: a numerical analysis. International Journal for Numerical and Analytical Methods in Geomechanics 27, 1207–1226. doi:10.1002/nag.314.

Peterson, J.W., Lindsay, A.D., Kong, F., 2018. Overview of the incompressible navier–stokes simulation capabilities in the MOOSE framework. Advances in Engineering Software 119, 68–92. doi:10.1016/j.advengsoft.2018.02.004.

Prodanovic, M., Esteva, M., Ketcham, R., Chang, B., Turhan, C., Gentle, J., Khan, S., Belcher, V., 2025. Digital porous media portal (dpmp) for publication, analysis, and simulation of porous media images. URL: https://doi.org/10.17612/FGMN-D889, doi:10.17612/FGMN-D889.

Rezaei, E., Zeinalzadeh, K., Ghanbarian, B., 2021. Experimental study of hydraulic properties in grain packs: Effects of particle shape and size distribution. Journal of Contaminant Hydrology 243, 103918. doi:10.1016/j.jconhyd.2021.103918.

Romano, P.K., Horelik, N.E., Herman, B.R., Nelson, A.G., Forget, B., Smith, K., 2015. Openmc: A state-of-the-art monte carlo code for research and development. Annals of Nuclear Energy 82, 90–97. doi:10.1016/j.anucene.2014.07.048.

Röding, M., Ma, Z., Torquato, S., 2020. Predicting permeability via statistical learning on higher-order microstructural information. Scientific Reports 10. doi:10.1038/s41598-020-72085-5.

Sadeghnejad, S., Reinhardt, M., Enzmann, F., Arnold, P., Brandstätter, B., Ott, H., Wilde, F., Hupfer, S., Schäfer, T., Kersten, M., 2023. Minkowski functional evaluation of representative elementary volume of rock microtomography images at multiple resolutions. Advances in Water Resources 179, 104501. URL: https://linkinghub.elsevier.com/retrieve/pii/S0309170823001367, doi:10.1016/j.advwatres.2023.104501.

Santaló, L.A., Kac, M., 2004. Integral Geometry and Geometric Probability. Cambridge University Press. doi:10.1017/cbo9780511617331.

Santos, J.E., Chang, B., Gigliotti, A., Yin, Y., Song, W., Prodanović, M., Kang, Q., Lubbers, N., Viswanathan, H., 2022. A dataset of 3d structural and simulated transport properties of complex porous media. Scientific Data 9. doi:10.1038/s41597-022-01664-0.

Saxena, N., Hows, A., Hofmann, R., Alpak, F.O., Dietderich, J., Appel, M., Freeman, J., De Jong, H., 2019. Rock properties from micro-ct images: Digital rock transforms for resolution, pore volume, and field of view. Advances in Water Resources 134, 103419. doi:10.1016/j.advwatres.2019.103419.

Schneider, R., 2014. Convex bodies. Number 151 in Encyclopedia of mathematics and its applications. 2nd expanded edition ed., Cambridge Univ. Press, Cambridge.

Scholz, C., Wirner, F., Götz, J., Rüde, U., Schröder-Turk, G.E., Mecke, K., Bechinger, C., 2012. Permeability of porous materials determined from the euler characteristic. Physical Review Letters 109, 264504. doi:10.1103/physrevlett.109.264504.

Sullivan, B., Kaszynski, A., 2019. PyVista: 3D plotting and mesh analysis through a streamlined interface for the Visualization Toolkit (VTK). Journal of Open Source Software 4, 1450. URL: https://doi.org/10.21105/joss.01450, doi:10.21105/joss.01450.

Tillmann, A., Englert, A., Nyari, Z., Fejes, I., Vanderborght, J., Vereecken, H., 2008. Characteriza-

tion of subsoil heterogeneity, estimation of grain size distribution and hydraulic conductivity at the krauthausen test site using cone penetration test. Journal of Contaminant Hydrology 95, 57–75. doi:10.1016/j.jconhyd.2007.07.013.

Vienken, T., Dietrich, P., 2011. Field evaluation of methods for determining hydraulic conductivity from grain size data. Journal of Hydrology 400, 58–71. doi:10.1016/j.jhydrol.2011.01.022.

van der Walt, S., Schönberger, J.L., Nunez-Iglesias, J., Boulogne, F., Warner, J.D., Yager, N., Gouillart, E., Yu, T., the scikit-image contributors, 2014. scikit-image: image processing in python. PeerJ 2, e453. doi:10.7717/peerj.453.

Zhao, X., Elsworth, D., He, Y., Hu, W., Wang, T., 2021. A grain texture model to investigate effects of grain shape and orientation on macro-mechanical behavior of crystalline rock. International Journal of Rock Mechanics and Mining Sciences 148, 104971. doi:10.1016/j.ijrmms.2021.104971.

Zhao, Z., Zhou, X.P., Qian, Q.H., 2020. Fracture characterization and permeability prediction by pore scale variables extracted from x-ray ct images of porous geomaterials. Science China Technological Sciences 63, 755–767. doi:10.1007/s11431-019-1449-4.

Zieba, Z., 2016. Influence of soil particle shape on saturated hydraulic conductivity. Journal of Hydrology and Hydromechanics 65, 80–87. doi:10.1515/johh-2016-0054.

Zwarts, S., Lesueur, M., 2024a. Homogenisation method based on energy conservation and independent of boundary conditions. Advances in Water Resources 183, 104603. URL: https://linkinghub.elsevier.com/retrieve/pii/S0309170823002385, doi:10.1016/j.advwatres.2023.104603.

Zwarts, S., Lesueur, M., 2024b. Predicting the Representative Elementary Volume by determining the evolution law of the convergence cone. Geomechanics for Energy and the Environment 40, 100594. URL: https://linkinghub.elsevier.com/retrieve/pii/S2352380824000613, doi:10.1016/j.gete.2024.100594.

Zwarts, S., Lindqwister, W., Lesueur, M., 2025. Rockmicro_minkowskis: A database of generated rock microstructures with minkowski functionals. https://github.com/sfzwarts/RockMicro_Minkowskis. Accessed: 2025-09-15.

Říha, J., Petrula, L., Hala, M., Alhasan, Z., 2018. Assessment of empirical formulae for determining the hydraulic conductivity of glass beads. Journal of Hydrology and Hydromechanics 66, 337–347. doi:10.2478/johh-2018-0021.